# Dynamic Response of Circular Concrete-filled Steel Tubular Columns under Very Low-elevation Lateral Impact Loads: Tests and Deflection Calculation Method

**Jiayu Liang**
Southwest Jiaotong University

**Yanhui Liu** ( ✉ yhliu@swjtu.edu.cn )
Southwest Jiaotong University

**Yichao Zhao**
China Construction Sixth Engineering Bureau Co., Ltd

**Nan Xu**
Southwest Jiaotong University

---

**Article**

**Keywords:**

**Additional Declarations:** No competing interests reported.

---

# Dynamic Response of Circular Concrete-filled Steel Tubular Columns under Very Low-elevation Lateral Impact Loads: Tests and Deflection Calculation Method

Jiayu Liang[1], Yanhui Liu[1,*] , Yichao Zhao[2], Nan Xu[1]

[1]School of Civil Engineering Southwest Jiaotong University, Chengdu 610031, PR China

[2]China Construction Sixth Engineering Bureau Co., Ltd., Tianjin 300012, PR China

[*]yhliu@swjtu.edu.cn

## Abstract

An experimental investigation of circular concrete-filled steel tubular (CFST) columns subjected to very low-elevation lateral impacts was performed. Six circular CFST members were prepared for lateral impact tests according to the typical CFST columns in high-speed railway stations in China. The impact location was at the height of the 2/9 column, which was determined according to the impact point between the running train and the column. There were three variables in the tests: the thickness of the steel tube, the impact velocity, and the axial load. The failure modes were determined in the tests, along with the time histories of the impact force and the deflection at the impact location. A finite-element analysis was performed to examine the effects of the axial load and scaling on the maximum deflection. According to the travelling plastic hinge theory, a three-stage rigid plastic mechanical model was employed to describe the impact process, in which the impact location was at the non-mid-span, and a calculation method for the deflection was developed. The method is generally applicable to CFST columns at any impact position. A comparison with the test results indicated that deflections can be calculated with reasonable accuracy using the proposed method.

## Introduction

Concrete-filled steel tubular (CFST) structures are widely used in civil engineering, e.g., in high-rise buildings, bridge piers, and underground infrastructures[1,2], because of their excellent performance[3-5]. CFST members play a significant role in the overall structure and have been used as protective components to resist extreme loads. During their period of service, structures may be subjected to lateral impact loads owing to accidental or intentional events, e.g., collisions with derailed trains, ships, or aircraft[6-8].

For the design of structures under lateral impact loads, several design codes[9-11] have offered general rules, in which the dynamic impact loads are simplified as equivalent static forces according to the type of vehicle. Undeniably, the real impact process is ignored in current design provisions. However, if more dynamic characteristics of the structure under impact are understood, a more precise design can be achieved.

Experimental[12-19] and numerical studies[12,13,16,17,20,21] have been performed on the behavior of CFST members under mid-span lateral impact loads since the beginning of the 21st century. According to extensive experiments, there are reasonable consensuses on the response characteristics associated with CFST members under mid-span lateral impact loads, which are summarized as follows. (1) Flexural failure is observed for all CFST members[12-19]. However, the confinement factor significantly affects the failure behavior[16]. Members with a large confinement factor exhibit ductility under the lateral impact, whereas those with a small one generally exhibits brittleness. (2) For the members exhibiting ductility, the failure is described as the local buckling is initiated in the contact area between the impactor and the members[12,15,16,19]; the global deformation begins at the mid-span of the members when the impact energy exceeds the local deformation energy; the steel tubes commonly undergo tensile fracture or rupture along the circumference; and the core concrete in the impact area is crushed under compression. (3) The impact force and the mid-span deflection are important parameters reflecting the response characteristics. Moreover, they are closely related to the impact speed, confinement factor, and boundary conditions[12-19]; however, compared with the impact force, the deflection is more significantly affected by the aforementioned factors[12]. (4) The global deformations consume most of the energy in the impact process, whereas the local deformations have low energy consumptio[12,18,19]. (5) The mid-span deflection and the impact force can be influenced by the axial load. When the initial impact velocity is low, the axial load can reduce the residual lateral deflection of the members, whereas when the initial velocity is high, the axial load can increase the deflection[16]. (6) The tube length does not affect the failure mode, but as the tube length increases, the local deformation increases, and the impact force decreases; thus, the tube length can affect the energy distribution between the local deformation and the global deformation[12,18]. Numerical studies on CFST members under impact loading have been conducted, such as those of Jia[12], Wang et al.[16], Bambach et al.[20], Remennikov et al.[14], Han et al[17], and Yousuf et al.[21].

Moreover, for members with flexural failure, the maximum deflection is an important index of the damage levels of the member subjected to impact[22,23] or the explosion loads[24] for developing guidelines for performance-based design[25] or design procedures[13]. Furthermore, members can be simplified using mass–spring–damper models[22]. Therefore, theoretical research has been performed on the calculation of the maximum deflection of members under lateral impacts. For CFST members, unified strength theory[2] and the theory of travelling plastic hinges[26,27] have been employed to develop a calculation method for the maximum deflection. For example, Jia[12] and Qu et al.[28] proposed a simplified deflection calculation method for CFST beams with simple supported and fixed-simple support conditions under mid-span lateral impact loads, respectively. Using Qu's model, Shakir et al.[18] derived a simplified deflection calculation formula for CFST members, in which the influence of the shape of the impactor was considered.

Furthermore, the axial load may affect the dynamic response of CFST columns. Experimental and numerical studies[29-32] have been performed on the behavior of CFST columns subjected to axial compression. Wang et al.[33] proposed a simplified calculation method, considering the effect of the axial load, based on the equivalent single-degree of freedom method for predicting the deflection of axially loaded CFST members subjected to lateral impacts.

Thus far, tests on CFST members (Table 1) have mostly employed scale models. Researchers have attempted to determine the dynamic response characteristics of a large prototype by testing a small model with a similar geometry. The similarity method is governed by certain principles, which may lead to differences in the dynamic response between the small model and the large prototype, i.e., the size effect. Booth[34] conducted 13 sets of drop hammer impact tests on sheet mild steel and structures ranging from ¼-size to full-scale and found that the dimensionless deflection of the full-scale prototype after the impact of the drop hammer was 2.5 times that of the small model, with a reduction coefficient of 0.25. Jones[27] deduced the similarity criterion between each physical parameter in the drop hammer impact test and proposed three physical phenomena that do not conform to the similarity relation: gravity, the strain-rate sensitivity of the material, and the fracture. For the drop hammer impact test, the acceleration may reach dozens of g during impact; thus, the gravitational acceleration has little effect on the test results. However, the other two factors may lead to differences in the dynamic response between the small model and the large prototype. Jin[35], utilizing numerical simulation methods, found that an increase in material strain rate weakens the influence of the lateral stress ratio on the size effect. Therefore, it is necessary to study the size effect.

In recent years, with the development of high-speed railway and road transportation, the threat of vehicle impacts on structures has increased, prompting some researchers[36-39] to focus on asymmetric impacts (where the impact location is not at the mid-span). However, compared with symmetric impacts, the dynamic response of CFST members under asymmetric impacts is not yet adequately understood. The recent numerical study of Alam[36], indicated that CFST columns exhibit flexible behavior with large global deformations at mid-height zones under the vehicular impact, which differs significantly from the results of the numerical simulations of Jia[12] and Wang's test study[39]. In Jia's study, the maximum deflection of the CFST members occurred at the impact location. Wang performed a series of tests on circular CFST columns under lateral impact loads. The impact location was 1/3H, the typical position of a vehicle (truck) impact, and the test results indicated that the CFST columns were prone to shear failure.

Detailed information regarding all the tests is presented in Table 1. In the boundary condition of the table, F stands for fixed, P stands for pinned and R stands for rolled.

**Table 1.** Details regarding research on the impact behavior of CFST members.

| No. | $D \times h \times L$ (mm × mm × mm) | Specimen number | Impact location | Boundary conditions | Researcher | Year |
|---|---|---|---|---|---|---|
| 1 | 114 × (3.5–4.5) × 1200 | 30 | 0.5L | F-F/P-P/F-P | Jia[12] | 2005 |
| 2 | (20–50) × 1.6 × 700 | 6 | 0.5L | P-P | Bambach et al.[13] | 2008 |
| 3 | 100 × 5 × 2500 | 2 | 0.5L | P-P | Remennikov et al.[14] | 2011 |
| 4 | 219 × 2.9 × (1880–3150) | 9 | 0.5L | P-P | Deng et al.[15] | 2012 |
| 5 | 114 × (1.7–3.5) × 1200 | 22 | 0.5L | F-F/P-P/F-P | Wang et al.[16] | 2013 |
| 6 | 100 × 5 × 2500 | 2 | 0.5L | R-P | Yousuf et al.[21] | 2013 |
| 7 | 180 × 3.65 × (1940–2800) | 9 | 0.5L | F-F/P-P/F-P | Han et al.[17] | 2014 |

| 8 | $114.3 \times (3\text{–}3.6) \times (686\text{–}1543)$ | 84 | 0.5L | F-F | Shakir et al. | 2016 |
| 9 | $114.3 \times 4.5 \times 1300$ | 3 | 0.5L | P-P | Alam et al. | 2017 |
| 10 | $300 \times 3.75 \times 1300$ | 9 | 0.3L | F-P | Wang et al. | 2017 |

Note: F-F = fixed–fixed; P-P = pinned–pinned; F-P = fixed–pinned; R-P = rolled–pinned.

At present, systematic research on the influence of asymmetry on CFST members remains limited. Kang[40] has developed an alternative modeling approach that effectively predicts the response of steel tube-concrete columns under low-velocity impact loads. Although the maximum deflection is considered as an important index for CFST members under lateral impact, no universal formula has been proposed for calculating the maximum deflection at any impact location for members. Therefore, an experimental investigation of CFST columns subjected to very low-elevation lateral impacts was conducted in this study. Six CFST members were designed based on the typical CFST columns in high-speed railway stations of China, and the impact location was determined according to the contact point between the running train and the column, as shown in Figure 1. The objectives of this paper were as follows: (1) to investigate the dynamic response of the members, including the failure mode, time-history curves of the impact force and deflection, and relationship between the impact force and the deflection; (2) to examine the effects of the axial load and scaling on the maximum deflection via finite-element analysis (FEA); and (3) to develop a rigid-plastic mechanical model for establishing a theoretical deflection calculation method that is generally applicable to CFST columns at any impact position.
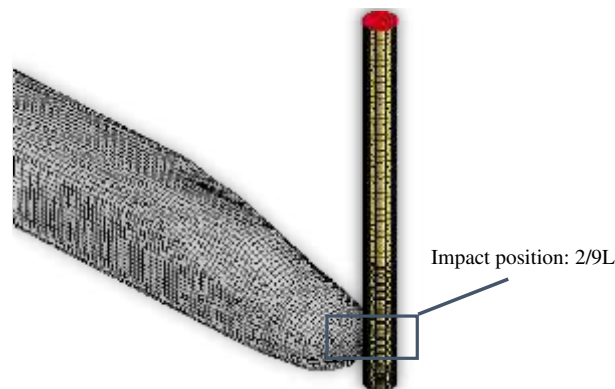


**Figure 1.** Schematic of the train impact column

| Notation | |
| --- | --- |
| $M$ | Impactor mass |
| $V_0$ | Initiation impact velocity |
| $l_1$ | Distance from right bearing to impact location |
| $l_2$ | Distance from left bearing to impact location |
| $L$ | Clear span of members |
| $m$ | Mass per unit length of members |
| $D$ | Outer diameter of circular steel tube |

| | |
|---|---|
| $h$ | Thickness of steel tube |
| $F$ | axial load |
| $f_y$ | Yield strength of steel |
| $f_c$ | Concrete cylinder compressive strength |
| $f_{cu}$ | Concrete cube compressive strength |
| $f_{ck}$ | Characteristic concrete strength |
| $\Delta$ | Test maximum deflection at impact location |
| $w_0$ | Predicted maximum deflection at impact location |
| $\eta$ | Geometric scale factor |

# Test

## Material properties

### Steel tubes

The steel tubes were fabricated using Chinese Standard Q235 steel. The Young's modulus ($E_s$) and the yield strength ($f_y$) were tested according to the Chinese Standard for metallic materials (GBT228-2002). The average yield strength of steel ($f_y$) are 338 MPa and 323 MPa for s 2.0-mm steel tube and 3.5-mm steel tube, respectively, and the corresponding modulus of elasticity ($E_s$) are 198 GPa and 223 GPa, respectively.

### Concrete

Nine $150 \times 150 \times 150$ mm$^3$ concrete cubes, which were cast and cured under the same conditions as the concrete used in the impact tests, were prepared to determine the concrete compressive strength of the specimens. The average measured cube strength of concrete at the day of testing is $f_{cu} = 54.97$ MPa.

## Test members and setup

To investigate the dynamic response of the CFST members under a non-mid-span impact, lateral impact tests were conducted using self-weight drop hammer impact testing equipment. Six sets of CFST specimens were designed and fabricated at a scale of 1:10, according to the typical CFST columns in the high-speed railway stations of China. Jones studied the scaling criteria of various parameters in the drop hammer impact test[27]. Table 2 presents the ratio of the physical parameters of the prototype to those of the model when the geometric ratio of the prototype to the scaled model was $\eta$ (in the tests, $\eta$ was 0.1). The ratios of the parameters shown in Table 2 were used to design the tests. Details regarding the specimens are presented in Table 3. The total length of the specimens was 1.5 m, with a clear span of 0.9 m. The

impact position for all the specimens was at 2/9 of the span, and the dimensions of the test segments are presented in Figure 2.

## Test apparatus

The lateral impact tests were performed using the DHR9401 drop hammer impact testing equipment. This equipment comprised the following segments: a test frame, a drop hammer, an impact head, supports at both ends, a load cell, and other ancillary equipment, as shown in Figure 3(a). The test frame was composed of a concrete foundation, rigid beams, and two steel columns, as shown in Figure 3(b). A drop hammer cast in forged steel, with a maximum impact height of 12.60 m, was employed, and the maximum impact velocity was 15.7 m/s, as shown in Figure 3(c). The test impact head, whose bottom surface was a rectangle with dimensions of $30 \times 80$ mm$^2$ and whose top surface was a circle with a diameter of 80 mm, was made of chromium 15 with 64HRC hardness, as shown in Figure 3(d). The boundary conditions were kept as a fixed support utilizing four different segments: the upper and lower half-rings were connected and fixed by bolts, the bottom of the support and bolts, as shown in Figure 3(e). An axial load loading device was equipped based on the drop hammer impact device, as shown in Figure 3(f).

The drop hammer was lifted to the design height and then released to impose the impact load. A high-speed camera (HSC) was employed to capture the failure modes of the specimens. The impact force was recorded by using a load cell built into the drop hammer.
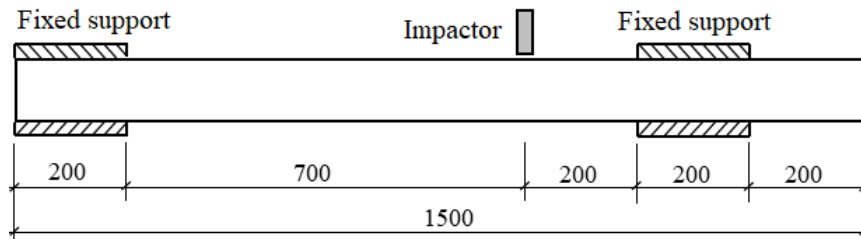


**Figure 2.** Member details and dimensions (unit: mm)

**Table 2.** Parameters in the prototype model relative to the reduced model.

| Parameter | Ratio | Parameter | Ratio |
| --- | --- | --- | --- |
| Geometric dimension | $\eta$ | Acceleration | $\eta^{-1}$ |
| Mass | $\eta^3$ | Time | $\eta$ |
| Material property | 1 | Force | $\eta^2$ |
| Velocity | 1 | Stress | 1 |

**Table 3.** Details of the test specimens.

| Specimen label | $M$ (kg) | $V_0$ (m/s) | $l_1$ (m) | $l_2$ (m) | $m$ (kg/m) | $D$ (mm) | $h$ (mm) | $F$ (kN) |
|---|---|---|---|---|---|---|---|---|
| YG1 | 270 | 7.67 | 0.2 | 0.7 | 31.3 | 114 | 2 | 0 |
| YG2 | 270 | 9.90 | 0.2 | 0.7 | 31.3 | 114 | 2 | 0 |
| YG3 | 270 | 11.71 | 0.2 | 0.7 | 31.3 | 114 | 2 | 0 |
| YG4 | 270 | 11.71 | 0.2 | 0.7 | 32.1 | 114 | 3.5 | 0 |
| TS1 | 270 | 9.90 | 0.2 | 0.7 | 32.1 | 114 | 3.5 | 0 |
| YG7 | 270 | 9.90 | 0.2 | 0.7 | 32.1 | 114 | 3.5 | 200 |
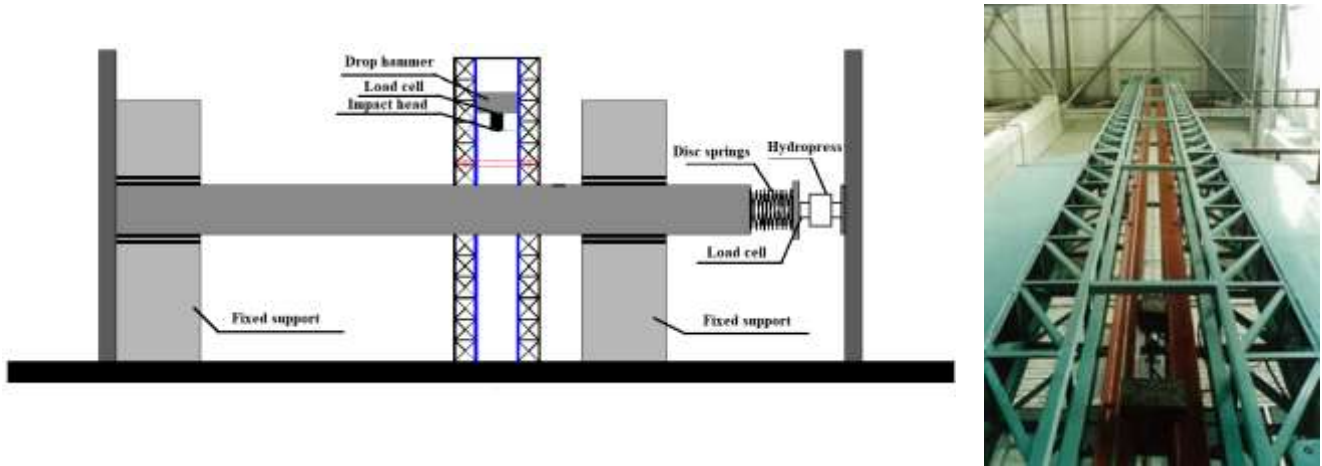


**(a)** Schematic of the impact test



**(b)** Test rack



**(c)** Drop hammer



**(d)** Impact head



**(e)** Fixed support



**(f)** Axial loading device

**Figure 3.** Drop hammer impact test device diagram

## Test results and discussions

### Failure modes

The final failure modes of the specimens were identified by analyzing the whole impact process, and the global deformation of the specimens is shown in Figure 4(a). All the specimens exhibited flexural failure, and the maximum deflection of the CFST members occurred at the impact location. Furthermore, flexural deformation occurred, but no cracks appeared in YG1, TS1, YG4, and YG7. Flexural cracks perpendicular to the axial direction of the members were observed in YG2. Although YG3 was completely fractured, it exhibited flexural cracks. The ultimate deformation mode under

the impact load included significant local compression deformations and buckling deformations at the impact point as well as at the edge of the supports, apart from the overall flexural deformation, as shown in Figure 4(b) and (c).

## Energy absorption

In the tests, the deflection-time curves were obtained using the HSC, and the force-time curves were obtained using a load cell built into the drop hammer. The results for the lateral force and lateral deflection are presented in Table 4. The force-time curves and deflection-time curves are shown in Figure 7 and Figure 8, respectively. The area beneath the force-displacement curve was used to calculate the recovered and absorbed energy, as shown in Figure 5. The ratio of the energy absorption to the total energy applied was then determined, as shown in Table 4.

**Table 4.** Test results.

| Specimen label | $\Delta$ (mm) | Maximum force (kN) | Absorbed energy (J) | Recovered energy (J) | Absorbed energy ratio |
|:---:|:---:|:---:|:---:|:---:|:---:|
| YG1 | 32.2 | 410.9 | 5432 | 367 | 93.7% |
| YG2 | Fracture | 449.6 | / | / | / |
| YG3 | Fracture | 527.1 | / | / | / |
| TS1 | 34.8 | 542.6 | 9204 | 937 | 92.4% |
| YG4 | 49.5 | 658.9 | 13950 | 422 | 97.1% |
| YG7 | 33.3 | 852.7 | 10100 | 538 | 94.7% |

Note: Absorbed energy ratio = absorbed energy / (absorbed energy + recovered energy)



**(a)** Global deformation of members



**(b)** Local deformation at the impact location



**(c)** Buckling deformation near supports

**Figure 4.** Failure modes of the tested members
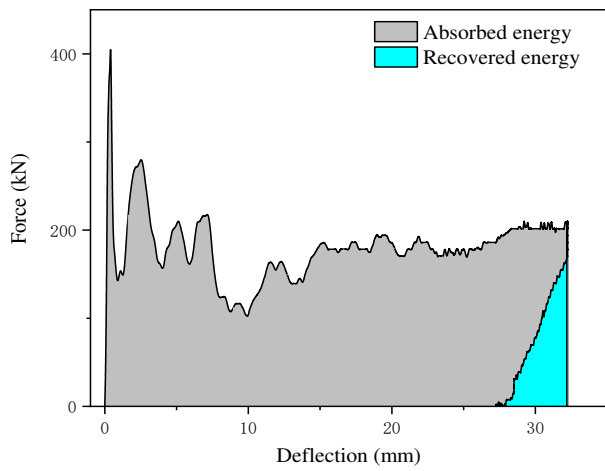
**(a)** YG1
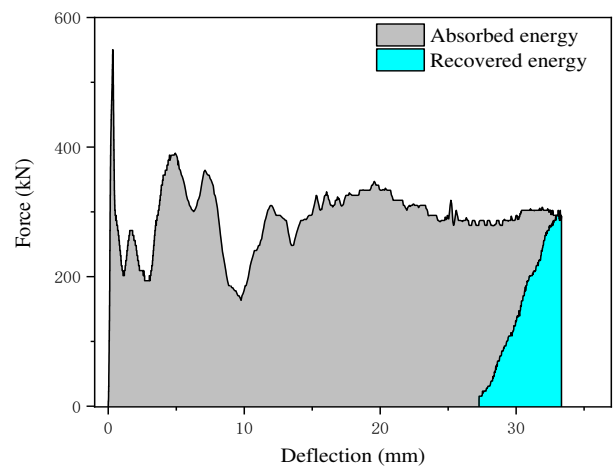


**(b)** TS1
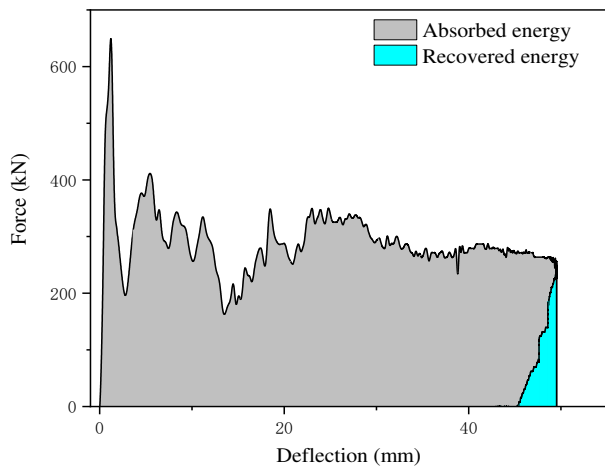


**(c)** YG4
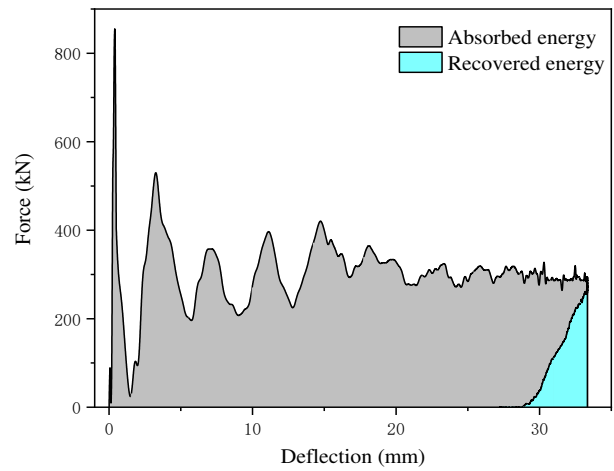


**(d)** YG7

**Figure 5.** Force–deflection curve

## Finite-element analysis

### Finite-element model

The commercial finite-element program LS-DYNA[41] was used to simulate the drop-weight impact test. Figure 6 shows the FEA model of the CFST member under the drop hammer impact. The drop hammer, steel tube, and core concrete were simulated using 8-node solid elements with reduced integration.

Regarding the material parameters, the properties of the concrete followed the concrete damage model, and the strain-rate effect of the concrete was considered according to the dynamic increase factor (DIF). The DIF for the compressive strength of concrete was defined by Malvar et al.[42] as follows:

$$\text{DIF} = \frac{f_{cd}}{f_{cs}} = \begin{cases} (\dot{\varepsilon}/\dot{\varepsilon}_s)^{1.026\alpha_s}, \dot{\varepsilon} \le 30s^{-1} \\ \gamma(\dot{\varepsilon}/\dot{\varepsilon}_s)^{1/3}, \dot{\varepsilon} > 30s^{-1} \end{cases}, \tag{1}$$

where $f_{cd}$ represents the dynamic compressive strength of the concrete at the strain rate $\dot{\varepsilon}$; $f_{cs}$ represents the static compressive strength of the concrete at the strain rate $\dot{\varepsilon}_s = 30 \times 10^{-6}$; $\log\gamma = 6.156\alpha_s - 2$; $\alpha_s = (5 + 9f_{cs}/f_{co})^{-1}$; and $f_{co} = 10$ MPa. The DIF for the tensile strength of concrete is given as

$$\text{DIF} = \frac{f_{td}}{f_{ts}} = \begin{cases} (\dot{\varepsilon}/\dot{\varepsilon}_s)^{1.016\delta_s}, \dot{\varepsilon} \le 30s^{-1} \\ \beta(\dot{\varepsilon}/\dot{\varepsilon}_s)^{1/3}, \dot{\varepsilon} > 30s^{-1} \end{cases}, \tag{2}$$

where $f_{td}$ represents the dynamic tensile strength of the concrete at the strain rate $\dot{\varepsilon}$; $f_{ts}$ represents the static tensile strength of the concrete at the strain rate $\dot{\varepsilon}_s = 30 \times 10^{-6}$; $\log\beta = 7.11\delta_s - 2.33$; and $\delta_s = (10 + 6f_{cs}/f_{co})^{-1}$. To simulate the failure of the concrete, the failure strain of the concrete was defined by MAT_ADD_EROSION in LS-DYNA. Malvar and Crawford proposed a DIF formulation for steel, with the yielding stress varying from 290 to 710 MPa[43]:

$$\text{DIF} = \frac{f_{yd}}{f_{ys}} = (\dot{\varepsilon}/10^{-4})^{\alpha}, \tag{3}$$

where $f_{yd}$ represents the dynamic yield strength of the steel at the strain rate $\dot{\varepsilon}$, $f_{ys}$ represents the static yield strength of the steel, and $\alpha = 0.074 - 0.040f_y/414$.

The impact body and the supports were regarded as rigid bodies without considering the influence of deformation. For the impact body and the supports, a rigid model was used. The keyword CONTACT_AUTOMATIC _SURFACE_TO_SURFACE was utilized to simulate the contact between the impact body and the specimen and that between the specimen and the support. The contact between the steel tube element and the concrete element was achieved using continuous nodes, and the relative slip was ignored. The axial load was applied to the transverse section as a uniform surface pressure, and the axial load was defined by DEFINE_CURVE, with its position and direction defined by LOAD_NODE_SET.
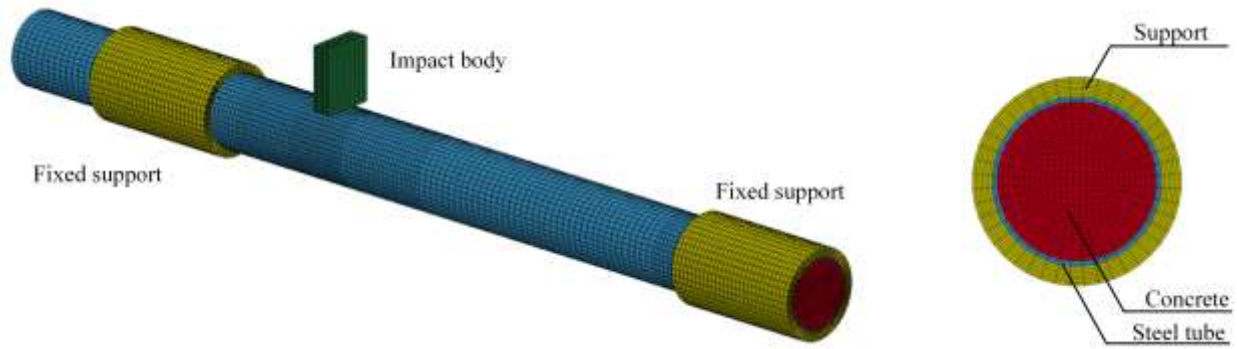
**Figure 6.** FEA model of the CFST member

## Comparison of simulation and test results

The impact-force time history curves and deflection time history curves are shown in Figure 7 and Figure 8, respectively, and the accuracy of the parameters used in the numerical simulation was verified via comparison with the test results. The trends of the impact-force and displacement time history curves were similar for the two groups of specimens. Detailed comparison results, including the maximum deflection, plateau valve of the impact force, and total duration, are presented in Table 5. Overall, the test and simulation results agreed well, and the errors were within a reasonable range, confirming the sufficient accuracy and precision of the parameters used in the simulation.

**Table 5.** Comparison between the simulation and test results

| Specimen | Maximum deflection (mm) | | | Plateau values of the impact forces (kN) | | | Total duration (s) | | |
|---|---|---|---|---|---|---|---|---|---|
| | Test | FEA | Error | Test | FEA | Error | Test | FEA | Error |
| YG1 | 32.2 | 31.1 | –3.40% | 209 | 223 | 6.70% | 0.0138 | 0.0133 | –3.60% |
| YG2 | / | / | / | 186 | 170 | –8.60% | / | / | / |
| YG3 | / | / | / | 202 | 186 | –7.92% | / | / | / |
| YG4 | 49.5 | 48.7 | –1.62% | 286 | 294 | 2.80% | 0.0131 | 0.0139 | 6.11% |
| YG7 | 33.3 | 32.4 | –2.70% | 288 | 320 | 11.1% | 0.0108 | 0.0109 | 0.93% |
| TS1 | 34.8 | 35.6 | 2.30% | 303 | 328 | 8.25% | 0.0116 | 0.0111 | –4.31% |
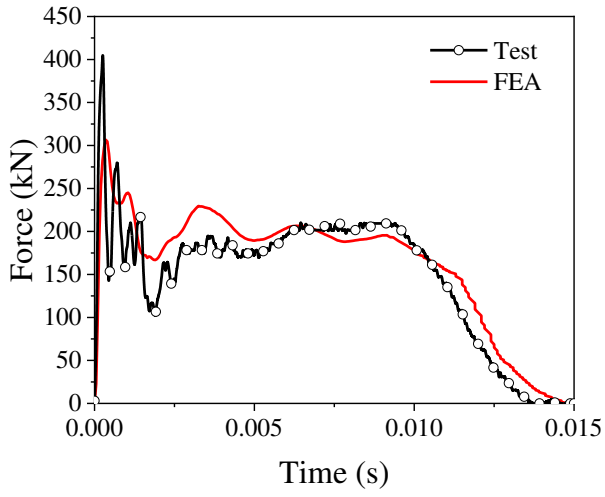
**(a)** YG1
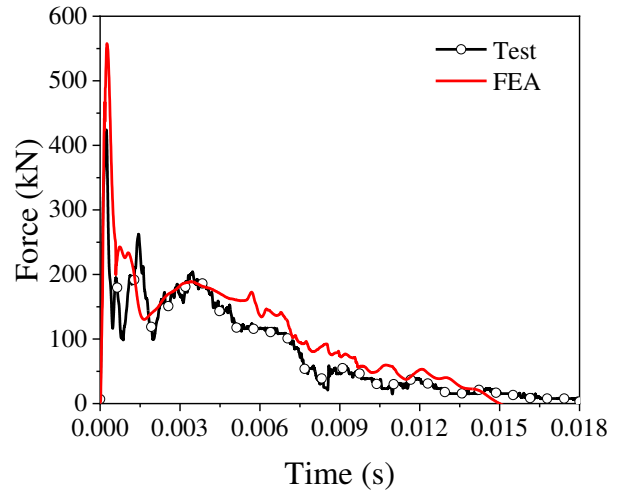
**(b)** YG2
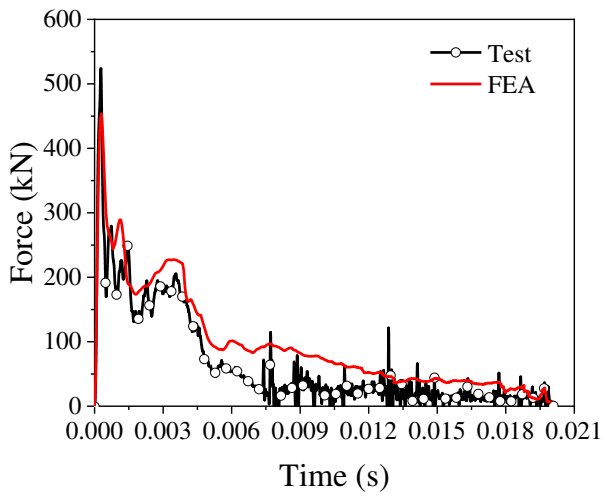
**(c)** YG3
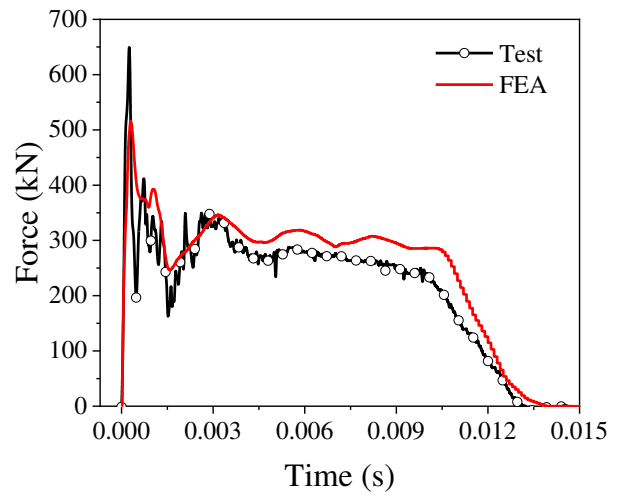
**(d)** YG4
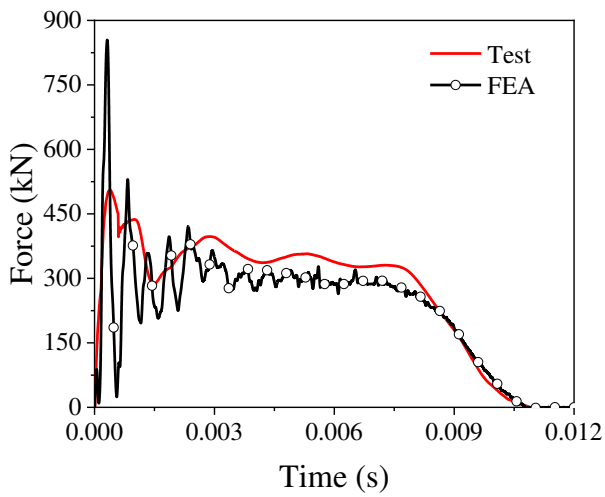
**(e)** YG7
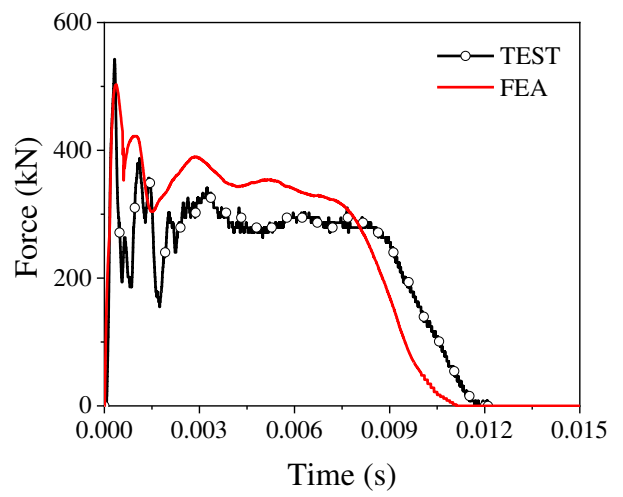
**(f)** TS1

**Figure 7.** Impact-force time history curves
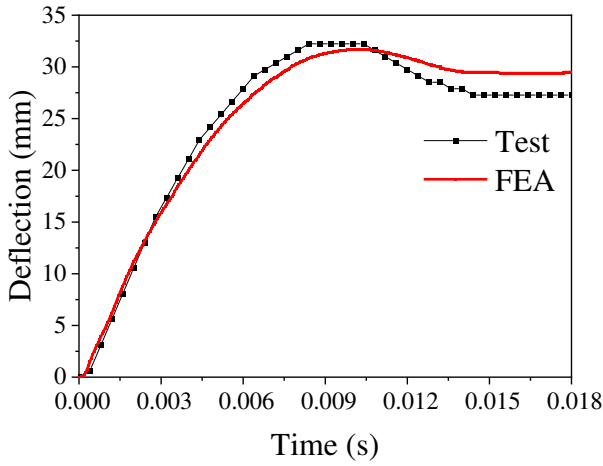
**(a)** YG1
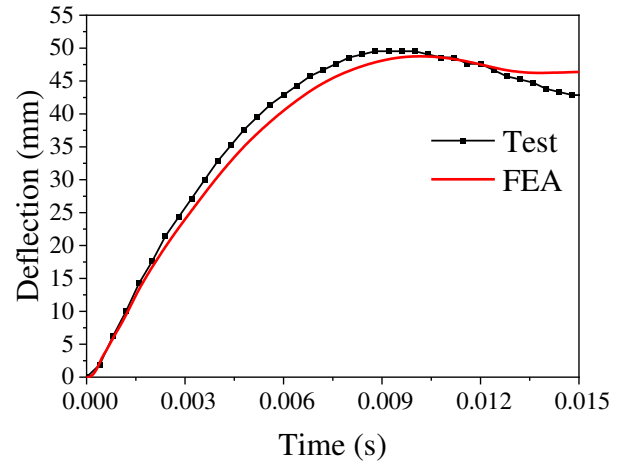
**(b)** YG4
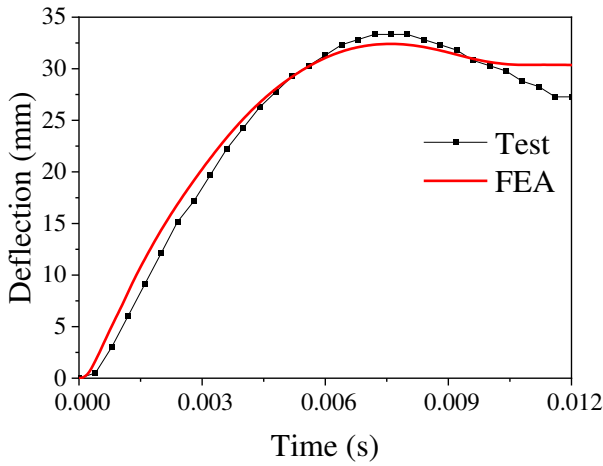
**(c)** YG7
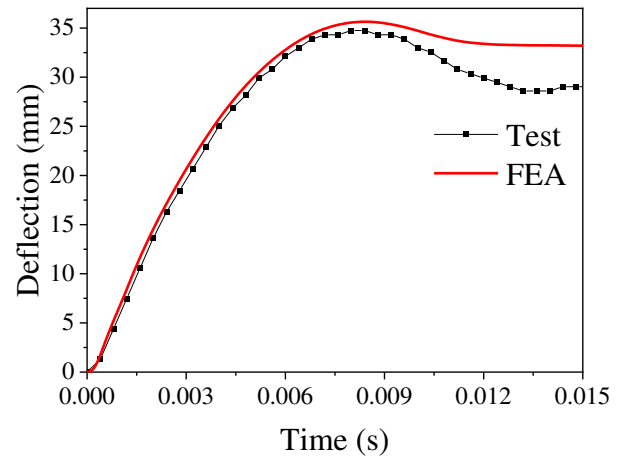
**(d)** TS1

**Figure 8.** Deflection time history curves

## Effect of axial load on deflection

The parameters of specimens TS1 and YG7 in the test were identical, except for the axial load. The maximum deflections of the two specimens were 34.8 and 33.3 mm, respectively (a small difference of 4.3%). This indicates that the axial load may have had only a slight effect on the deflection of the unbroken member. To describe the effect of the axial load more accurately, the impact processes of TS1 components under different axial compression ratios were supplemented using LS-DYNA software (Table 6). As shown in Figure 9, with an increase in the axial compression ratio, the maximum deflection of the CFST members first decreased and then increased. When the axial compression ratio was approximately 0.4, the deflection was minimized. When the axial compression ratio was approximately 0.8, the deflection was close to that without an axial load. When the axial pressure was <0.8, the axial load improved the lateral impact resistance of the CFST members. When the axial compression ratio was >0.8, the axial load reduced the lateral impact resistance of the CFST members. Under different axial compression ratios, the maximum deflections of the members were close (within 10%).

13

**Table 6.** Effect of the axial compression ratio on the deflection

| Axial compression ratio | 0 | 0.1 | 0.2 | 0.3 | 0.4 | 0.5 | 0.6 | 0.7 | 0.8 | 0.9 |
|---|---|---|---|---|---|---|---|---|---|---|
| Maximum deflection | 35.6 | 33.7 | 32.6 | 32.2 | 32.1 | 32.5 | 33.1 | 34.1 | 35.8 | 36.9 |
| Error | 0 | -5.3% | -8.4% | -9.6% | -9.8% | -8.7% | -7.0% | -4.2% | 0.56% | 3.65% |
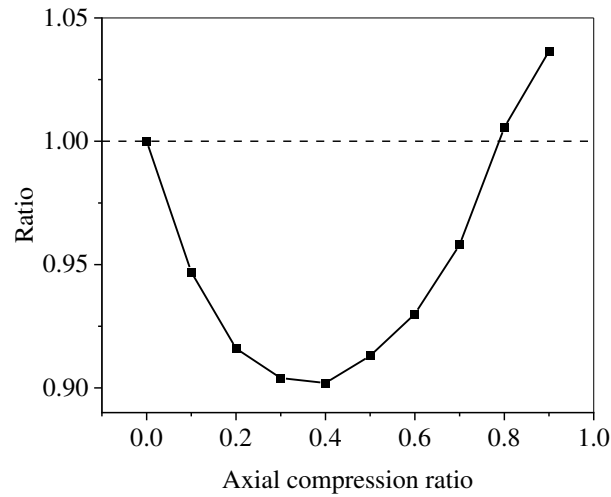


**Figure 9.** Relationship between the deflection and the axial compression ratio

## Scaling effect on deflection

The response of CFST members under the impact of the lateral drop hammer involves multiple physical quantities, and the relationships between these physical quantities can be determined via dimensional analysis. The physical quantities that determine the maximum deflection $w_0$ mainly include the

(1) impact body parameters, i.e., impact body mass $M$, density $\rho_I$, impact surface area $S$, and impact velocity $V_0$;

(2) concrete material properties, i.e., density $\rho_c$, elastic modulus $E_c$, compressive strength $f_c$, and Poisson's ratio $\mu_c$;

(3) material properties of steel, i.e., density $\rho_s$, elastic modulus $E_s$, yield strength $f_y$, and Poisson's ratio $\mu_s$; and

(4) component geometry, i.e., outer diameter of the circular steel tube $D$, thickness of the steel tube $h$, distance $l_1$ from the impact point to the left support, and distance $l_2$ from the impact point to the right support.

According to the foregoing 16 physical quantity parameters, the functional relationship between the maximum deflection and each physical quantity can be expressed as follows:

$$w_0 = f(M, \rho_I, S, V_0, \rho_c, E_c, f_c, \mu_c, \rho_s, E_s, f_y, \mu_s, h, D, l_1, l_2), \tag{4}$$

Three physical parameters with independent dimensions—the cross-sectional diameter $D$ of the member, the

elastic modulus of the steel $E_s$, and the density of the steel $\rho_s$—are selected as the basic quantities. Equation (5) can be derived from equation (4) based on the $\pi$ theorem:

$$\frac{w_0}{D} = a_0 \left( \frac{M}{\rho_s D^3} \right)^{a_1} \left( \frac{\rho_l}{\rho_s} \right)^{a_2} \left( \frac{S}{D^2} \right)^{a_3} \left( V_0 \sqrt{\frac{\rho_s}{E_s}} \right)^{a_4} \left( \frac{\rho_c}{\rho_s} \right)^{a_5} \left( \frac{E_c}{E_s} \right)^{a_6}$$
$$\left( \frac{f_c}{E_s} \right)^{a_7} \left( \mu_c \right)^{a_8} \left( \frac{f_y}{E_s} \right)^{a_9} \left( \mu_s \right)^{a_{10}} \left( \frac{h}{D} \right)^{a_{11}} \left( \frac{l_1}{D} \right)^{a_{12}} \left( \frac{l_2}{D} \right)^{a_{13}} \quad , \tag{5}$$

where $a_0$–$a_{13}$ are real numbers to be determined.

Equation (5) provides a general calculation model for such problems and is suitable for the establishment of empirical models for maximum deflection calculation with different steel and concrete materials, different geometric parameters, and different impact conditions.

When the parameters in the model and the prototype are set to the values presented in Table 2, the relationship between the model and the prototype can be expressed as

$$\left( \frac{w_0}{D} \right)_m = \left( \frac{w_0}{D} \right)_p , \tag{6}$$

where the subscripts m and p represent the model (small-scale experiment) and the prototype (full-scale experiment), respectively.

Equation (6) indicates that when parameters are set in strict accordance with the similarity theory, as shown in Table 2, the deflection of the components in the scaled steel tube concrete drop weight impact test conforms with the similarity criterion. To further verify the similarity, an FEA model of each component in the experiment was established, as well as one of the full-scale prototype components. Then, $\eta w - \eta t$ curves obtained from finite-element calculations were compared ($\eta = 0.1$ for the prototype component and $\eta = 1$ for the model component), as shown in Figure 10. The deflection variations of the prototype and the model exhibited the same trend, confirming that the deflection of the component satisfied the assumption of the similarity theory. Table 7 shows that the deflection error between the scaled-down model and the full-scale prototype falls within the 7%. Consequently, the size effect was ignored in this experiment.

**Table 7.** Size effect on the deflection

| Specimen | YG1 | PYG1 | YG4 | PYG4 | YG7 | PYG7 | TS1 | PTS1 |
|---|---|---|---|---|---|---|---|---|
| $\eta w_0$(mm) | 31.1 | 32.8 | 48.7 | 51.9 | 32.4 | 32.7 | 32.7 | 32.5 |
| Error | 5.47% | | 6.57% | | 0.93% | | -0.61% | |

## Velocity variation at impact point

The lateral velocity variation at the impact point of the specimens, caused by the lateral impact, is shown in Figure 11. At the beginning of the impact, the velocity increased sharply to the maximum value in a very short time. Then, the velocity decreased nearly linearly with respect to time. Because the impact force was

essentially stable after a short fluctuation in the initial stage of impact (Figure 7), its acceleration was also stable, eventually leading to a linear decrease in the velocity over time. When the velocity decreased to zero, the specimen reached the maximum deflection.

## Moment variation at impact point

The moment variation at the impact point of the specimens, caused by the lateral impact, is shown in Figure 12. At the beginning of the impact, the moment increased sharply to the ultimate value in a very short time. Then, the moment decreased to a certain value and remained at this value for a relatively long time, covering the main period of the impact. This moment can be defined as the ultimate plastic moment capacity. The dynamic ultimate plastic moment capacity $M_{dp}$, obtained from LS-DYNA, is presented in Table 8.



**(a)** YG1

**(b)** YG4

**(c)** YG7

**(d)** TS1
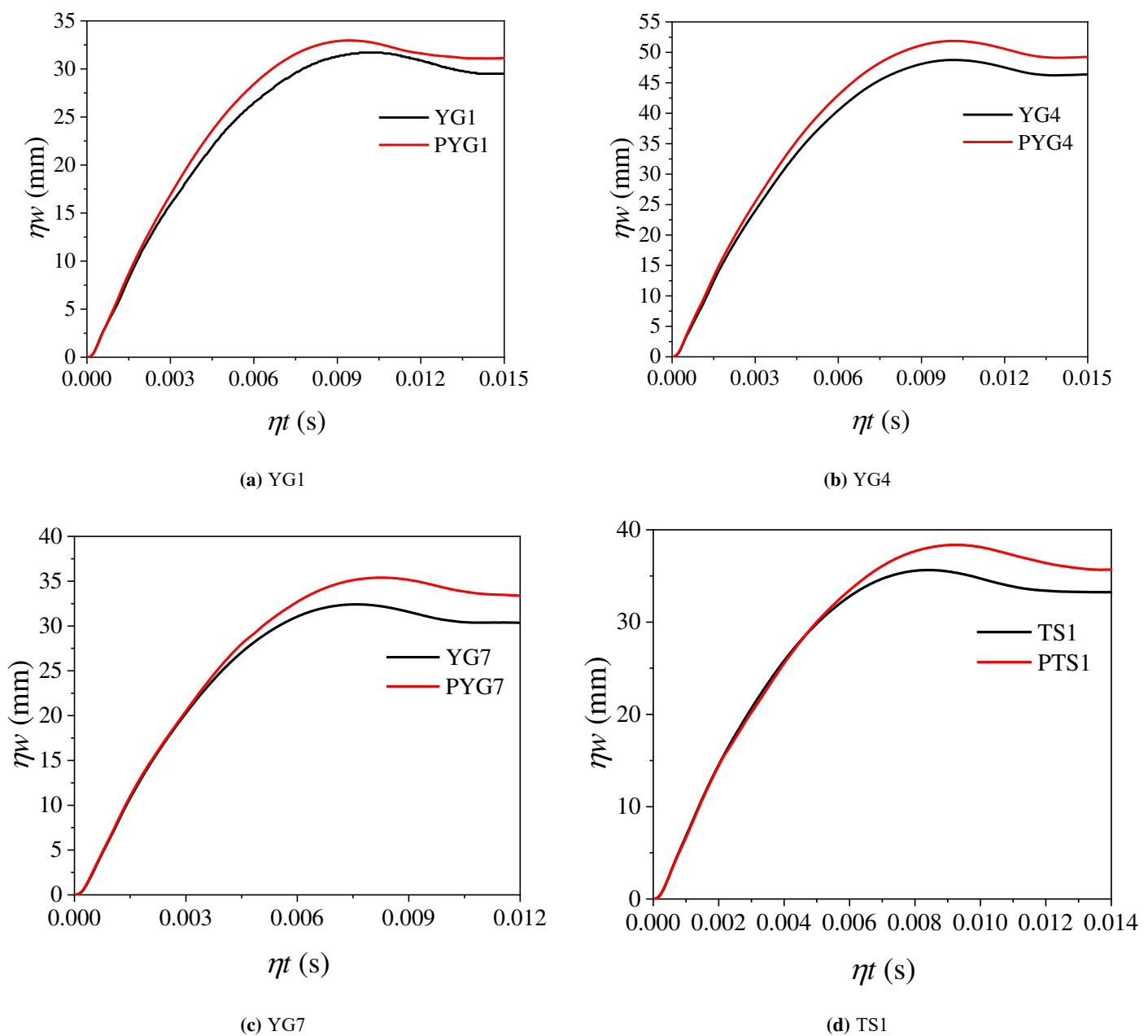
**Figure 10.** $\eta w - \eta t$ curves
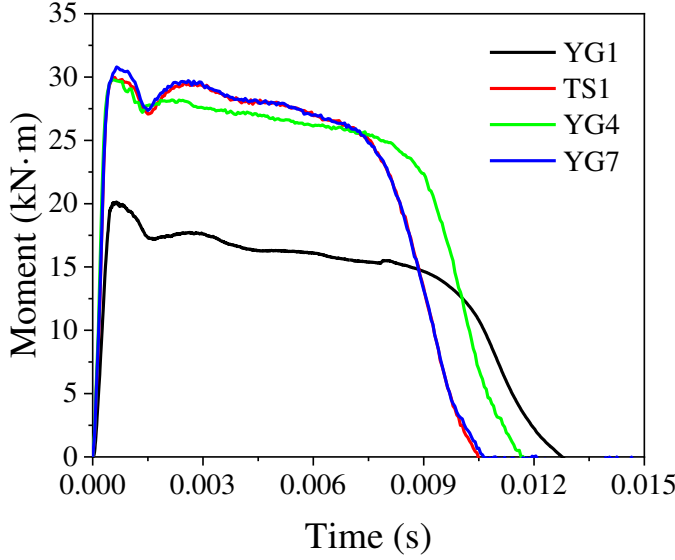
**Figure 11.** Impact point cross-section moment history from LS-DYNA
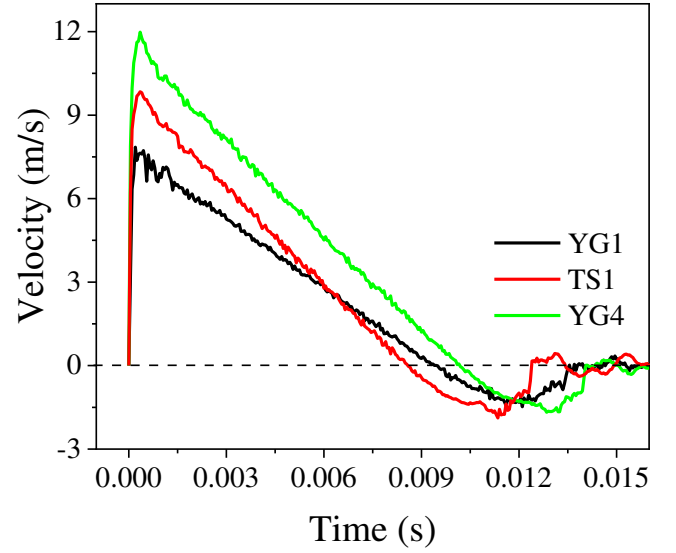


**Figure 12.** Impact velocity history from LS-DYNA

## Proposed calculation method

### Ultimate plastic moment capacity

In this analysis, the ultimate plastic moment $M_p$ is an important parameter. Elchalakani et al. presented a simplified rigid plastic approach for determining the ultimate plastic moment capacity of circular CFST members[44], which can be expressed as follows:

$$M_p = \frac{2}{3} f_c \left( \frac{D}{2} - h \right)^3 \cos^3 \gamma_0 + 4 f_y \left( \frac{D-h}{2} \right)^2 h \cos \gamma_0, \tag{7}$$

Here, $\gamma_0$ represents the angular location of the plastic neutral axis. It can be calculated as

$$\gamma_0 = \frac{\dfrac{\pi}{4} \dfrac{f_c (D/2-h)^2}{f_y (D/2-h/2)h}}{2 + \dfrac{f_c (D/2-h)^2}{f_y (D/2-h/2)h}}, \tag{8}$$

$M_p$ represents the static ultimate plastic moment. Based on $M_p$, the dynamic ultimate plastic moment $M_{dp}$ can be expressed as

$$M_{dp} = \lambda_1 \frac{2}{3} f_c \left( \frac{D}{2} - h \right)^3 \cos^3 \gamma_0 + 4 \lambda_2 f_y \left( \frac{D-h}{2} \right)^2 h \cos \gamma_0 \tag{9}$$

$$\gamma_0 = \frac{\dfrac{\pi}{4}\dfrac{\lambda_1 f_c \left(D/2 - h\right)^2}{\lambda_2 f_y \left(D/2 - h/2\right)h}}{2 + \dfrac{\lambda_1 f_c \left(D/2 - h\right)^2}{\lambda_2 f_y \left(D/2 - h/2\right)h}}, \tag{10}$$

where $\lambda_1$ and $\lambda_2$ represent the DIFs for concrete and steel, respectively, at the rotation rate $\dot{\theta}$. DIFs $\lambda_1$ and $\lambda_2$ can be determined using equations (1)-(3) when the rotation rate is $\dot{\theta}$. As discussed in Velocity variation at impact point, assuming that the lateral velocity of the impact point decreases linearly over time, the rate of rotation $\dot{\theta}$ of the mid-span section is defined as follows:

.
$$\dot{\theta} = \dot{\theta}_1 + \dot{\theta}_2 = \frac{V_0}{2l_1} + \frac{V_0}{2l_2}, \tag{11}$$

Table 8 presents the static ultimate plastic moment $M_p$ of the specimens (calculated using equations (7) and (8)) and the dynamic ultimate plastic moment ($^1M_{dp}$ was obtained from LS-DYNA, and $^2M_{dp}$ was calculated using equations (9)–(11)). The slight discrepancy between $^1M_{dp}$ and $^2M_{dp}$ confirms the accuracy of the calculation method.

**Table 8.** Ultimate plastic moment capacity

| Specimen | $M_p$ (kN·m) | $^1M_{dp}$ (kN·m) | $^2M_{dp}$ (kN·m) | $M_{dp}^2/M_{dp}^1$ |
|---|---|---|---|---|
| YG1 | 10.8 | 16.0 | 17.5 | 1.09 |
| TS1 | 16.4 | 27.7 | 26.5 | 0.96 |
| YG4 | 16.4 | 26.7 | 26.9 | 1.01 |
| YG7 | 16.4 | 27.7 | 26.5 | 0.96 |

## Three phases of motion

Jones[27] theoretically derived the dynamic response of a beam under a mid-span impact with fixed–fixed supports. Wang[45] has theoretically deduced the dynamic response of rigid-plastic structures subjected to lateral impact at an arbitrary point and divided their motion process into three phases. According to Wang's research, a rigid-plastic model and the travelling plastic hinge theory were adopted to calculate the deflection of an arbitrary impact point on the CFST members in this study.

The basic mechanical model is shown in Figure 13(a). A member with a length of $l_1 + l_2$ is under a lateral impact at an arbitrary point O by a mass $M$ with an initial velocity $V_0$. The impact point travels with a velocity $V_0$ at the instant of impact while the rest of the member remains stationary. Therefore, the disturbance at the impact point propagates to both supports of the member. Then, global bending deformation occurs, dissipating the remaining impact energy, and finally ceases. This impact process can be divided into three distinct phases of motion, hereinafter referred to as the first, second, and third phases of motion. In this analysis, the influence of the axial load is neglected, and it is considered that the yield shear force of the cross-section is sufficiently large to prevent slippage.

(a) Impact model             (b) First phase of motion

(c)   Second phase of motion         (d) Third phase of motion
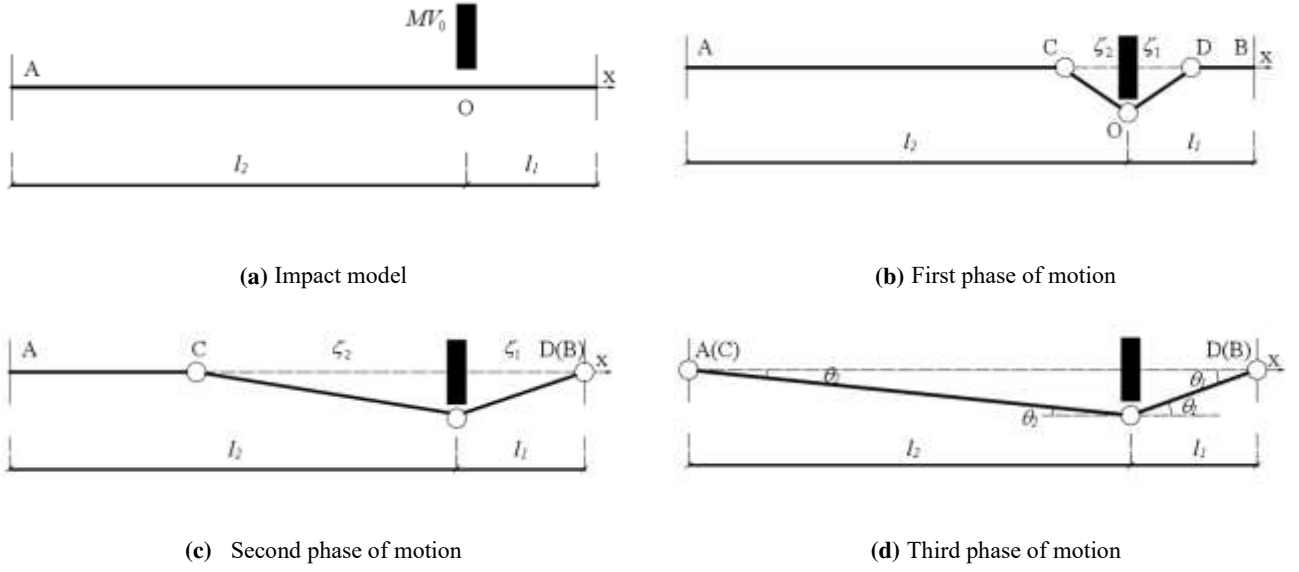
**Figure 13.** Impact process

## First phase of motion

As shown in Figure 13(b), in the first phase of motion, a plastic hinge develops at the impact point at $t = 0$, and two other plastic hinges propagate the disturbance away from the impact point toward the two supports. Then, travelling plastic hinge D reaches support B, forming a stationary plastic hinge.

O is taken as the origin of the coordinate system, and the positive direction of the X-axis is to the right. The lateral velocity field at an arbitrary point of the member in the first phase of motion is expressed as follows:

$$\dot{w} = \begin{cases} \dot{w}_0\left(1 + x/\varsigma_2\right), \left(-\varsigma_2 \le x < 0\right) \\ \dot{w}_0\left(1 - x/\varsigma_1\right), \left(0 \le x < \varsigma_1\right) \\ 0, \left(-l_2 \le x < -\varsigma_2, \varsigma_1 \le x \le l_1\right) \end{cases}, \tag{12}$$

where $\varsigma_1$ and $\varsigma_2$ represent the time-dependent locations of travelling plastic hinges D and C, respectively, and $\dot{w}_0$ represents the lateral velocity at the impact point.

Taking half of the member for analysis, the moments of impact point O are given as follows:

$$2M_{dp} - \int_0^{\varsigma_1} m\ddot{w}x\,dx = 0 \tag{13}$$

$$2M_{dp} - \int_{-\varsigma_2}^{0} m\ddot{w}x\,dx = 0, \tag{14}$$

Combining equations (13) and (14) yields $\varsigma_1 = \varsigma_2$.

Because the lateral shear force is zero at the travelling plastic hinges where the maximum bending moment develops, the vertical equilibrium for the central portion of the member between the two travelling plastic hinges C and D demands that

19

$$M\ddot{w}_0 + \int_{-\zeta_2}^{\zeta_1} m\ddot{w}dx = 0 , \tag{15}$$

After equation (12) is substituted into equation (15), integrating equation (15) with respect to time and using the initial conditions $\dot{w}_0 = 0$ and $\zeta_1 = 0$ at $t = 0$ yields

$$\dot{w}_0 = V_0 / \left(1 + m\zeta_1 / M\right), \tag{16}$$

Substituting equation (12) into equation (13) yields

$$\int_0^{\zeta_1} m[\ddot{w}_0 \left(1 - x / \zeta_1\right) + \dot{w}_0 x \dot{\zeta}_1 / \zeta_1^2]xdx = 2M_{dp} , \tag{17}$$

which can be written in the following form:

$$d(\dot{w}_0 \zeta_1^2) / dt = 12M_{dp} / m , \tag{18}$$

Finally, integrating equation (18) with respect to time and using the initial conditions $\zeta_1 = 0$ at $t = 0$ yields the location-time characteristic of the travelling plastic hinge:

$$t = \frac{MmV_0\zeta_1^2}{12M_{dp}\left(M + m\zeta_1\right)} , \tag{19}$$

Taking the derivative of equation (19) with respect to time predicts the velocity of the travelling plastic hinge:

$$\dot{\zeta}_1 = \frac{12M_{dp}(M + m\zeta_1^2)^2}{Mm\zeta_1 V_0(2M + m\zeta_1)} , \tag{20}$$

At the end of the first phase of motion ($t = t_1$), the lateral deflection of the first phase of motion at the impact point $w_{01}$ can be described through the following equation:

$$w_{01} = \int_0^{t_1} \dot{w}_0 dt = \int_0^{l_1} \dot{w}_0 d\dot{\zeta}_1 / \dot{\zeta}_1 , \tag{21}$$

Substituting equations (16) and (20) into equation (21) yields

$$w_{01} = \frac{M^2 V_0^2}{24M_{dp}m}\left[2\ln\left(\frac{ml_1 + M}{M}\right) + \frac{M^2}{\left(M + ml_1\right)^2} - 1\right], \tag{22}$$

## Second phase of motion

As shown in Figure 13(c), in the second phase of motion, after plastic hinge D becomes a stationary hinge, plastic hinge C continues moving toward support A until reaching it and forms a stationary plastic hinge.

In the second phase of motion, the bending moment at plastic hinge D may no longer be the extreme

point in the bending-moment diagram; thus, there is a nonzero shear force $Q$ at plastic hinge D. Additionally, $\zeta_1 = l_1$. The lateral velocity field in the second phase of motion can be expressed as follows:

$$
\dot{w} = \begin{cases}
\dot{w}_0\left(1 + x/\zeta_2\right), & \left(-\zeta_2 \le x < 0\right) \\
\dot{w}_0\left(1 - x/l_1\right), & \left(0 \le x \le l_1\right) \\
0, & \left(-l_2 \le x < -\zeta_2\right)
\end{cases}
\tag{23}
$$

As shown in Figure 14, the force balance can be expressed as:

$$
\begin{cases}
\dfrac{m}{2}\left(\zeta_2\ddot{w}_0 + \dot{\zeta}_2\dot{w}_0\right) = Q_2 \\[2mm]
\dfrac{m}{2}l_1\ddot{w}_0 = Q_1 - Q
\end{cases},
\tag{24}
$$
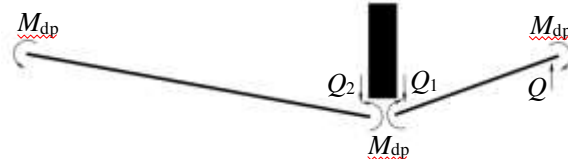


**Figure 14.** Force analysis diagram

where $Q_1$ and $Q_2$ represent the shear forces on the left and right sides of O, respectively; and $Q$ represents the shear force at plastic hinge D. The bending-moment balance can be expressed as:

$$
\begin{cases}
\dfrac{m}{12}\zeta_2\left(\zeta_2\ddot{w}_0 - \dot{\zeta}_2\dot{w}_0\right) = \dfrac{1}{2}\zeta_2 Q_2 - 2M_{dp} \\[2mm]
\dfrac{m}{12}l_1^2\ddot{w}_0 = \dfrac{1}{2}l_1\left(Q_1 + Q\right) - 2M_{dp}
\end{cases}.
\tag{25}
$$

Combining equation (24) and equation (25) yields

$$
\left(\dfrac{1}{3}ml_1^2 + Ml_1\right)\ddot{w}_0 + \dfrac{1}{2}ml_1\left(\zeta_2\ddot{w}_0 + \dot{\zeta}_2\dot{w}_0\right) = -2M_{dp}
\tag{26}
$$

$$
m\zeta_2\left(\zeta_2\ddot{w}_0 + 2\dot{\zeta}_2\dot{w}_0\right) = 12M_P.
\tag{27}
$$

Integrating equations (26) and (27) with respect to time and using the continuous conditions at $t_1$ yield

$$
\left(\dfrac{1}{3}ml_1^2 + Ml_1 + \dfrac{1}{2}ml_1\zeta_2\right)\dot{w}_0 = -2M_{dp}t + Ml_1 V_0
\tag{28}
$$

$$
m\zeta_2^2\dot{w}_0 = 12M_{dp}t.
\tag{29}
$$

By combining equations (28) and (29), the velocity at the impact point can be determined as follows:

$$
\dot{w}_0 = \dfrac{6Ml_1 V_0}{2ml_1^2 + 6Ml_1 + 3ml_1\zeta_2 + m\zeta_2^2}.
\tag{30}
$$

The velocity of the traveling plastic hinge can be predicted by substituting equation (30) into equation (29) and then integrating equation (29) with respect to time:

$$\dot{\zeta}_2 = \frac{2M_{dp}(2ml_1^2 + 6Ml_1 + 3ml_1\zeta_2 + m\zeta_2^2)^2}{Mml_1V_0(3ml_1\zeta_2^2 + 4ml_1^2\zeta_2 + 12Ml_1\zeta_2)} .$$  (31)

Integrating the velocity with respect to time yields

$$w_{02} = \int_{t_1}^{t_2} \dot{w}_0 dt = \int_{l_1}^{l_2} \dot{w}_0 d\zeta_2 / \dot{\zeta}_2 ,$$  (32)

where $w_{02}$ represents the lateral deflection of the second phase at the impact location.

Substituting equations (30) and (31) into equation (32) yields

$$w_{02} = \frac{3M^2ml_1^2V_0^2}{M_{dp}} \int_{l_1}^{l_2} \frac{3ml_1\zeta_2^2 + 4ml_1^2\zeta_2 + 12Ml_1\zeta_2}{(2ml_1^2 + 6Ml_1 + 3ml_1\zeta_2 + m\zeta_2^2)^3} d\zeta_2 .$$  (33)

## Third phase of motion

As shown in Figure 13(d), in the third phase of motion, the plastic hinges at the support and the impact location remain stationary, and the member continues moving downward under the action of the impact energy until the kinetic energy of the member and the impactor is exhausted. The third phase of motion is the final phase of the dynamic response of the CFST member under the impact. According to the rigid-plastic dynamic model, it is assumed that all the remaining kinetic energy of the impactor and member are consumed by plastic deformation in this phase.

According to motion analysis for the first and second phases of motion, as well as the kinetic energy theorem, the kinetic energy of span $l_2$ and span $l_1$ can be calculated as follows:

$$K_2^{l_2} = \int_{-l_2}^{0} \frac{1}{2}m\left[\frac{6Ml_1V_0}{2ml_1^2 + 6Ml_1 + 3ml_1l_2 + ml_2^2}(1 + x/l_2)\right]^2 dx = \frac{6mM^2l_1^2l_2V_0^2}{(2ml_1^2 + 6Ml_1 + 3ml_1l_2 + ml_2^2)^2}$$  (34)

$$K_2^{l_1} = \int_{0}^{l_1} \frac{1}{2}m\left[\frac{6Ml_1V_0}{2ml_1^2 + 6Ml_1 + 3ml_1l_2 + ml_2^2}(1 - x/l_1)\right]^2 dx = \frac{6mM^2l_1^3V_0^2}{(2ml_1^2 + 6Ml_1 + 3ml_1l_2 + ml_2^2)^2} .$$  (35)

The kinetic energy of the impactor is given as follows:

$$K_1 = \frac{1}{2}M\left[\frac{6Ml_1V_0}{2ml_1^2 + 6Ml_1 + 3ml_1l_2 + ml_2^2}\right]^2 = \frac{18M^3l_1^2V_0^2}{(2ml_1^2 + 6Ml_1 + 3ml_1l_2 + ml_2^2)^2} .$$  (36)

The total kinetic energy of the system is the sum of the kinetic-energy values of the member and the impactor:

$$K = K_1 + K_2^{l_1} + K_2^{l_2} = \frac{18M^3 l_1^2 V_0^2 + 6mM^2 l_1^2 V_0^2 (l_1 + l_2)}{(2ml_1^2 + 6Ml_1 + 3ml_1 l_2 + ml_2^2)^2} . \tag{37}$$

According to the assumption for the third phase of motion, the energy-balance principle, and the rigid-plastic model, all the kinetic energy of the system is dissipated by the plastic hinge. Then,

$$2M_{dp}\theta_1 + 2M_{dp}\theta_2 = K , \tag{38}$$

where $\theta_1$ and $\theta_2$ represent the angle of rotation of travelling plastic hinges D and C, respectively.

From the lateral deflection field and the geometric relationship of the member, the following equation can be obtained:

$$\theta_1 l_1 = \theta_2 l_2 . \tag{39}$$

By combining equations (37)-(39), the lateral deflection of the third phase at the impact location $w_{03}$ can be calculated as follows:

$$w_{03} = \frac{18M^3 l_1^3 l_2 V_0^2 + 6mM^2 l_1^3 l_2 V_0^2 (l_1 + l_2)}{M_{dp}(2l_1 + 2l_2)(2ml_1^2 + 6Ml_1 + 3ml_1 l_2 + ml_2^2)^2} . \tag{40}$$

By unifying the calculations and analyses for the three phases of motion, a theoretical deflection calculation equation for CFST members constraints was obtained:

$$w_0 = w_{01} + w_{02} + w_{03} \tag{41}$$

Equation (41) was used to calculate the deflection of the impact points of YG1, TS1, and YG4 under the lateral impact, and the results are presented in Table 9. The calculation errors of the method were <8%, which satisfies the accuracy requirements of engineering.

**Table 9.** Deflection of the members

| Specimen label | $\Delta$ (mm) | $w_0$ (mm) | Error |
|---|---|---|---|
| YG1 | 32.2 | 34.08 | 5.8% |
| TS1 | 34.8 | 37.53 | 7.9% |
| YG4 | 49.5 | 51.69 | 4.4% |

## Error analysis

Based on the ideal rigidity-plasticity of materials and the theory of travelling plastic hinges, a method for calculating the deflection at the impact point of CFST members was developed. In the theoretical derivation, a simplified rigid-plastic model was applied, with the assumption that all the energy is completely dissipated by the plastic hinges. Nevertheless, in the actual case where CFST members bear a lateral impact, the materials are not rigid-plastic as supposed; thus, not all the energy is absorbed by the members, as shown in Figure 5 and Table 4. Furthermore, local compression deformation, steel tube buckling deformation at the edge of the support, and friction energy dissipation at the restraint end can also consume energy, as shown in Figure 4. Therefore, the energy during the impact process is not entirely dissipated by plastic deformation.

## Conclusions

The following conclusions are drawn based on the research presented in this paper:

(1)  Lateral non-mid-span impact tests of CFST specimens were performed. It was found that: ① the global deformation and flexural cracks indicated that the specimens underwent flexural failure; ② the maximum deflection of CFST columns appeared at the impact location under very low-elevation lateral impact loads; ③ the maximum deflection is an essential index for CFST members under lateral impacts, which is related to the impact velocity and the thickness of the steel tube; ④ the recovered and absorbed energy were calculated by integrating the force-displacement curve, and the absorbed energy ratio was >90%.

(2)  A FEA was performed for further study, revealing the following. ① The axial load had no significant effect on the transverse deflection of the specimens. With an increase in the axial compression ratio, the deflection tended to decrease and then increase, but the axial load had little influence on the transverse deflection (within 10%). ② The deflection of the model and prototype conforms to the similarity criterion if the specimen is designed strictly according to the similarity criterion. Therefore, the size effect on the transverse deformation can be ignored (within 6%). ③ The bending moment at the impact point of the specimen increases sharply after impact. After fluctuation, it remains stable at a certain value, that is, the ultimate plastic moment of the specimen. ④ The lateral velocity at the impact point decreases linearly before the maximum deflection of the specimen is reached.

(3)  According to the travelling plastic hinge theory and the assumption of the ideal rigid-plastic model, the motion of CFST members subjected to lateral impact can be divided into three phases. Accordingly, a mechanical analysis of the CFST member during each phase was performed to calculate the deflection of the member, and a corresponding theoretical method was proposed.

## References

1       Shanmugam, N. E. & Lakshmi, B. State of the art report on steel–concrete composite columns. *Journal of Constructional Steel Research* **57**, 1041-1080, doi:10.1016/s0143-974x(01)00021-9 (2001).

2       Han L. *The structure of steel tube filled concret.* Vol. 7 (Beijing: Science Press, 2000). (in Chinese)

3       Morino, S., Uchikoshi, M. & Yamaguchi, I. Concrete-filled steel tube column system-its advantages. *Steel Structures* **1**, 33-44 (2001).

4       Morino, S. & Tsuda, K. Design and construction of concrete-filled steel tube column system in Japan. *Earthquake Engineering and Engineering Seismology* **4**, 51-73 (2003).

5       Starossek, U., Falah, N. & Lohning, T. Numerical analyses of the force transfer in concrete-filled steel tube columns. *Structural Engineering and Mechanics* **35**, 241-256, doi:10.12989/SEM.2010.35.2.241 (2010).

6       Grob, J. & Hajdin, N. Train Derailment and Its Impact on Structures. *Structural Engineering International* **3**, 88-94, doi:10.2749/101686693780612484 (1993).

7       A. Knott, M. in *Ship Collision Analysis*      (ed Henrik Gluver)    75-84 (Routledge, 2017).

8       Thai, D.-K. & Kim, S.-E. Safety assessment of a nuclear power plant building subjected to an aircraft crash. *Nuclear Engineering and Design* **293**, 38-52, doi:10.1016/j.nucengdes.2015.07.053 (2015).

9       En. Eurocode 1: Actions on structures-Part 1-7: General actions-Accidental actions. *European Committee for Standardization* **54**, 18-20 (2006).

10      En, B. S. 2. Eurocode 1: Actions on Structures–Part 2: Traffic Loads on Bridges. *British Standard Institution, UK: London* (2003).

11      Design-Build, T. O. J. T. C. o. *American Association of State Highway and Transportation Officials Guide for Design-build Procurement.*    (AASHTO, 2008).

12      Jia D. *The accidence research of steel tube-confined concrete in the lateral impact*, Taiyuan University of Technology, (2005).(in Chinese)

13      Bambach, M. R., Jama, H., Zhao, X. L. & Grzebieta, R. H. Hollow and concrete filled steel hollow sections under transverse impact loads. *Engineering Structures* **30**, 2859-2870, doi:10.1016/j.engstruct.2008.04.003 (2008).

14      Remennikov, A. M., Kong, S. Y. & Uy, B. Response of Foam- and Concrete-Filled Square Steel Tubes under Low-Velocity Impact Loading. *J. Perform. Constr. Facil.* **25**, 373-381, doi:10.1061/(ASCE)CF.1943-5509.0000175 (2011).

15      Deng, Y., Tuan, C. Y. & Xiao, Y. Flexural Behavior of Concrete-Filled Circular Steel Tubes under High-Strain Rate Impact Loading. *J. Struct. Eng.* **138**, 449-456, doi:10.1061/(ASCE)ST.1943-541X.0000464 (2012).

16      Wang, R., Han, L.-H. & Hou, C.-C. Behavior of concrete filled steel tubular (CFST) members under lateral impact: Experiment and FEA model. *Journal of Constructional Steel Research* **80**, 188-201, doi:10.1016/j.jcsr.2012.09.003 (2013).

17      Han, L., Hou, C., Zhao, X. & Rasmussen, K. J. Behaviour of high-strength concrete filled steel tubes under transverse impact loading. *Journal of Constructional Steel Research* **92**, 25-39 (2014).

18      Shakir, A., Guan, Z. & Jones, S. Lateral impact response of the concrete filled steel tube columns with and without CFRP strengthening. *Engineering structures* **116**, 148-162 (2016).

19      Alam, M. I. *et al.* Performance and dynamic behaviour of FRP strengthened CFST members subjected to lateral impact. *Engineering Structures* **147**, 160-176 (2017).

20      Bambach, M. R. Design of hollow and concrete filled steel and stainless steel tubular columns for transverse impact loads. *Thin-Walled Structures* **49**, 1251-1260, doi:10.1016/j.tws.2011.05.009 (2011).

21      Yousuf, M., Uy, B., Tao, Z., Remennikov, A. & Liew, R. Behaviour and resistance of hollow and concrete-filled mild steel columns due to transverse impact loading. *Australian Journal of Structural Engineering* **13**, 65-80 (2012).

22      Fujikake, K., Li, B. & Soeun, S. Impact Response of Reinforced Concrete Beam and Its Analytical Evaluation. *J. Struct. Eng.* **135**, 938-950, doi:10.1061/(ASCE)ST.1943-541X.0000039 (2009).

23      Fujikake, K., Senga, T., Ueda, N., Ohno, T. & Katagiri, M. Study on Impact Response of Reactive Powder Concrete Beam and Its Analytical Model. *J. Struct. Eng.* **135**, 938-950, doi:10.3151/jact.4.99 (2009).

24      Krauthammer, T., Muralidharan, R. & Schmidt, W. Combined Symbolic-Numeric Explosion Damage Assessment for Structures. *Journal of Computing in Civil Engineering* **6**, 417-434, doi:10.1061/(ASCE)0887-3801(1992)6:4(417) (1992).

25      Tachibana, S., Masuya, H. & Nakamura, S. Performance based design of reinforced concrete beams under impact. *J. Struct. Eng.* **4**, 938-950, doi:10.5194/nhess-10-1069-2010 (2009).

26      Lee, E. H. & Symonds, P. S. Large Plastic Deformations of Beams Under Transverse Impact. *Journal of Applied Mechanics* **19**, 308-314, doi:10.1115/1.4010503 (1952).

27      Jones, N. *Structural impact.*    (Cambridge university press, 2011).

28      Qu, H., Li, G., Chen, S., Sun, J. & Sozen, M. Analysis of Circular Concrete-Filled Steel Tube Specimen

under Lateral Impact. *Advances in Structural Engineering* **14**, 941-952, doi:10.1260/1369-4332.14.5.941 (2011).

29    Ravi Kumar, H., Muthu, K. U. & Kumar, N. S. Study on Predicting Axial Load Capacity of CFST Columns. *Journal of Computing in Civil Engineering* **99**, 133-140, doi:10.1007/s40030-017-0234-y (2018).

30    Sevim, B. Structural response of rectangular composite columns under vertical and lateral loads. *Steel and Composite Structures* **25**, 287-298, doi:10.12989/SCS.2017.25.3.287 (2017).

31    Li, P., Zhang, T. & Wang, C. Behavior of Concrete-Filled Steel Tube Columns Subjected to Axial Compression. *Advances in Materials Science and Engineering* **2018**, 1-15, doi:10.1155/2018/4059675 (2018).

32    Ravi Kumar, H. *et al.* Behavior of Concrete-Filled Steel Tube Columns Subjected to Axial Compression. *Advances in Materials Science and Engineering* **2018**, 1-15, doi:10.1155/2018/4059675 (2018).

33    Wang, L. *et al.* Deflection calculation based on SDOF method for axially loaded concrete-filled steel tubular members subjected to lateral impact. *Shock and Vibration* **2020**, 1-16 (2020).

34    Booth, E., Collier, D. & Miles, J. Impact scalability of plated steel structures. *Structural crashworthiness*, 136-174 (1983).

35    Jin, L., Li, J., Yu, W. & Du, X. Size effect modelling for dynamic biaxial compressive strength of concrete: Influence of lateral stress ratio and strain rate. *International Journal of Impact Engineering* **156**, 103942 (2021).

36    Alam, M. I., Fawzia, S. & Zhao, X.-L. Numerical investigation of CFRP strengthened full scale CFST columns subjected to vehicular impact. *Engineering Structures* **126**, 292-310, doi:10.1016/j.engstruct.2016.07.058 (2016).

37    Demartino, C. *et al.*

38    Gurbuz, T., Ilki, A., Thambiratnam, D. P. & Perera, N. Low-Elevation Impact Tests of Axially Loaded Reinforced Concrete Columns. *ACI Structural Journal* **116**, doi:10.14359/51710862 (2019).

39    Wang X., Demartino, C., Xu J,. & Xiao Y. Dynamic response of concrete filled steel column under lateral impact:test study and calculation method. *China civil engineering journal* **50**, 28-36, doi:10.15951/j.tmgcxb.2017.12.004 (2017). (in Chinese)

40    Kang, L., Fan, W., Liu, B. & Liu, Y. Numerically efficient analysis of concrete-filled steel tubular columns under lateral impact loading. *Journal of Constructional Steel Research* **179**, 106564, doi:10.1016/j.jcsr.2021.106564 (2021).

41    Hallquist, J. O. LS-DYNA Keyword Users Manual–Nonlinear Dynamic Structural Analysis of Structures. *Livermore Software Technology Corporation (LSTC)* (1999).

42    Malvar, L. J., Crawford, J. E., Wesevich, J. W. & Simons, D. A plasticity concrete material model for DYNA3D. *International Journal of Impact Engineering* **19**, 847-873, doi:10.1016/S0734-743X(97)00023-7 (1997).

43    Malvar, L. J. & Crawford, J. E. Dynamic increase factors for concrete. *DTIC document* **1**, 1.6 (1998).

44    Elchalakani, M., Zhao, X.-L. & Grzebieta, R. H. Concrete-filled circular steel tubes subjected to pure bending. *Journal of constructional steel research* **57**, 1141-1168 (2001).

45    Wang R. *Study on the dynamic response and damage failure of concrete filled steel tube under lateral impact*, Taiyuan University of Technology, (2008). (in Chinese)

## Acknowledgements

## Author contributions

Conceptualization, Y.L; Methodology, J.Y and Y.Z; Software, N.X; Data curation, J. Y; Validation, N.X; Visualization, Y.Z; Writing- Original draft preparation, J.Y; Writing - Review & Editing, J.Y; Funding acquisition, Y.L; Supervision, Y.L. All authors have read and agreed to the published version of the manuscript.

## Data availability

The datasets used and analyzed during the current study are available from the corresponding author upon reasonable request.

## Competing interests

The authors declare no competing interests.